NON-INTRUSIVE MODEL ORDER REDUCTION FOR SINTERING APPLICATIONS

RAHUL DHOPESHWAR[∗], HARSHIT BANSAL[∗], HAO SHI[†], DILETTA GIUNTINI[†] AND KAREN VEROY[∗]

[∗] Department of Mathematics and Computer Science
[†] Department of Mechanical Engineering
Eindhoven University of Technology, 5612 AZ Eindhoven, The Netherlands
e-mail: r.dhopeshwar@tue.nl

Key words: Macroscopic Sintering, Non-Intrusive Model Order Reduction, Proper Orthogonal Decomposition, Gaussian Process Regression, Thermo-mechanical Coupled Problems

Abstract. We are interested in thermo-mechanical problems arising in the context of a practically relevant manufacturing process called sintering. These models can be defined using a non-linear material model, namely the Skorohod-Olevsky Viscous Sintering (SOVS) constitutive model. This SOVS model is used to predict macroscopic sintering behavior, such as shrinkage and density evolution. Also, it relies on material properties such as temperature-dependent viscosity and surface tension. However, high-fidelity simulations of coupled, macroscopic, thermo-mechanical models are computationally intensive. Furthermore, developing reduced-order models addressing the non-linearities is challenging due to the history dependence and presence of internal variables. Performing parametric studies, optimization, real-time control, or parameter estimation for such problems, thus, becomes infeasible. In order to accelerate sintering simulations for such multi-query scenarios, a surrogate model is vital. Here, we present a non-intrusive reduced-order modelling framework based on proper orthogonal decomposition and Gaussian process regression. Furthermore, we discuss the performance of such a surrogate model using different metrics for the two-parameter Arrhenius-type viscosity function.

1 INTRODUCTION

Sintering is a manufacturing process where powdered material is consolidated into a solid at high temperatures with or without applied pressure [7]. It is mainly used for manufacturing ceramics, metal-oxides, and metals with high melting points. Lately, there has been a growing interest in controlling the sintering process in view of its ability to manufacture materials with desirable functional properties [16], applications in 3D printing [15], etc. Usually, this process is controlled based on heuristic knowledge and experimental trial and error. However, this can lead to complications such as shape distortion and cracks, resulting in a waste of time, energy, and material. Predicting the shrinkage behavior and stress state of the material during the whole sintering process is thus important to avoid such issues and control the (final) properties of the sintered product. This demands predictive computational sintering models [1].

Sintering is, in general, a multi-scale, multi-physics process. It can be simulated at different length scales [25]. At the atomistic scale, molecular dynamics simulations [2] can be

used to model material diffusion during sintering. However, these methods require enormous computational effort and are infeasible for scales beyond tens of nanometers. At the micro- or meso-scale, numerical methods, such as the discrete element method, the kinetic Monte Carlo method, and phase-field methods [23], are suitable for the thermo-mechanical modelling of the sintering process. In particular, these methods are useful to predict microstructure morphology evolution during sintering but fail to connect this to macroscopic behavior, which entails predicting shrinkage, distortions, etc., that are relevant to a variety of industrial problems. However, only macro-scale (process) parameters can be controlled during the sintering process. The finite element-based continuum-based models, in conjunction with phenomenological constitutive laws, such as the Skorohod-Olevsky Viscous Sintering (SOVS) model [20], are well-known to be better equipped in predicting the macroscopic sintering behavior and investigating shape distortion and stress concentrations. Given this knowledge and the overarching goal of designing microstructures, estimating important microstructural parameters, or controlling (macroscopic) process parameters for the desired macroscopic response, in this work, we study coupled macroscopic continuum-based models.

In the past, attempts have been made to use the macro-scale, coupled, multi-physics model for the design and optimization of the process parameters, material, and geometry; see [8, 9]. It is generally regarded that a single finite element simulation of a coupled (single-scale) macro, multi-physics model, governed using the SOVS constitutive law, is computationally expensive. Also, extensive studies pertaining to design, optimization, and process control require numerous such simulations. Aiming to significantly reduce computational efforts, in [26], a methodology has been proposed to accelerate the simulation of viscous sintering at the macroscopic level. However, the proposed finite element simulation, despite being faster than the state-of-the-art approaches, remains computationally expensive for multi-query design and optimization. Furthermore, in [29], the authors employ principal component analysis and Gaussian process autoregressive models to develop reduced-order microstructure representation and accelerate the prediction of microstructure evolution, which is usually computed using expensive phase-field models. However, such a technique has not yet been employed at the macro-scale for the thermo-mechanical coupled problem governed by the SOVS constitutive model. Hence, there is a need to: *(i)* speed up the (macro-scale) sintering model simulations in a multi-query scenario, and *(ii)* accelerate the inverse estimation of hard-to-measure sintering (process) parameters, such as viscosity and surface tension.

In order to overcome the aforementioned limitations in the scope of sintering, in this work, we resort to projection-based model order reduction (MOR) techniques that have been shown to provide significant speed-ups for several other challenging, industrially relevant applications; see [4, 19, 27]. As is well known, the efficacy of the reduced-order model is determined by the computational cost's independence from the full-order dimension in the online phase. The classical MOR techniques [21] fail to achieve this for non-linear problems with affine or non-affine parametric dependence as they still involve expensive full-order assembly in the online phase. Hyper-reduction techniques [11, 17, 27] address this issue. Recently, such hyper-reduction techniques have also been employed to accelerate relevant problems in the scope of additive manufacturing; see [6, 19]. However, these hyper-reduction techniques are, in general, problem-dependent and intrusive in nature and, hence, require a thorough understanding and access to various components of the numerical method used for full-order simulations. Moreover, several works [5, 8, 9] often rely on commercial software, for predictive modelling. Herein, one

does not have access to all the details of the underlying numerical methods. Intrusive MOR techniques, as mentioned above, which rely on access to the underlying numerical method and assembled matrices, are impractical in these scenarios. To this end, many non-intrusive MOR techniques, such as Physics-informed machine learning techniques [3], regression-based approaches like POD-GPR [12], deep neural network-based methods, e.g., Deep-HyROMnet [4], etc., have recently been proposed to develop a surrogate model in a purely data-driven way. Such methods are essential in the scope of predictive modelling of manufacturing processes like sintering and can leverage the existing modelling knowledge that builds on (not so openly accessible) commercial codes.

In this work, we are interested in the sintering of a 3D ZnO powder compact, since it is widely used in many electrical and electronic applications like varistors, piezoelectric devices, etc. [22]. This process is governed by a coupled thermo-mechanical model, together with the SOVS model that can easily be extended to coupled systems and used for modelling advanced sintering techniques, such as field-assisted sintering, spark plasma sintering, ultra-fast high-temperature sintering, etc. [9]. In past works, different temperature-dependent material viscosity functions, defining the SOVS model, have been proposed, and have subsequently been used for analyzing the deformation, stress, strain, and density evolution of the material undergoing sintering. For instance, initial revisions of the SOVS model propose polynomial viscosity functions that capture the viscosity evolution well in a certain temperature range. Arrhenius-type viscosity functions, as in [24], which are based on (empirical) data fitting, capture thermal activation phenomena of the sintering process, and are applicable for wider temperature ranges. Here, for exhaustive design and optimization studies, we parametrize the Arrhenius-type temperature-dependent viscosity function using two parameters and develop a non-intrusive reduced-order model using POD-GPR for enabling multi-query investigations in the context of sintering.

2 MODEL FORMULATION FOR SINTERING

The sintering process is modeled using a continuum mechanics-based macroscopic model with the SOVS constitutive law. It is governed by a coupled system of partial differential equations where we simultaneously solve for the displacement, temperature, and density fields.

2.1 Governing conservation equations: strong form

Given a 3D material domain Ω and a time domain $\tau \equiv [0, t_{\mathrm{f}}]$, where t_{f} is the final time, the evolution of the relative density field $\rho : \Omega \times \tau \to [0, 1]$ is governed by the continuity equation,

$$\dot{\rho} + \rho \dot{e} = 0, \tag{1}$$

where $\dot{e}$ is the volumetric strain rate and $\dot{\rho}$ is the temporal derivative of the relative density. The temperature field $T : \Omega \times \tau \to \mathbb{R}$ is governed by the transient heat conduction equation,

$$\frac{\partial T}{\partial t} - \nabla \cdot (\alpha_{\mathrm{T}} \nabla T) = 0, \tag{2}$$

where α_{T} is the thermal diffusivity of the material being sintered. The linear momentum balance is described by:

$$\nabla \cdot \underline{\sigma} = 0, \tag{3}$$

where the Cauchy stress tensor, denoted by $\underline{\sigma}$, depends on the displacement field $u : \Omega \times \tau \to \mathbb{R}^3$. This balance equation is used to solve for the displacement field in a quasi-static sense. The acceleration of the material displacement and the thermal expansion of the material is ignored in this work. Furthermore, additional body forces or external forces are not considered.

2.2 Constitutive model

The linear viscous model formulation of the SOVS model is typically used to describe free sintering (i.e., without any applied pressure) or sintering of non-crystalline (amorphous) material. The sintering behavior is described by the decomposition of the strain into elastic and viscous (inelastic) components:

$$\underline{\varepsilon} = \underline{\varepsilon}^{\text{el}} + \underline{\varepsilon}^{\text{in}}. \tag{4}$$

The corresponding strain rates follow:

$$\underline{\dot{\varepsilon}} = \underline{\dot{\varepsilon}}^{\text{el}} + \underline{\dot{\varepsilon}}^{\text{in}}. \tag{5}$$

The volumetric strain rate in the mass-balance equation, i.e., (1), is given by $\dot{e} = tr(\underline{\dot{\varepsilon}}^{\text{in}})$. The stress $\underline{\sigma}$ relates to the elastic strain by Hooke's law,

$$\underline{\sigma} = \lambda_1 \nabla \cdot u \underline{\mathrm{I}} + 2\lambda_2 \underline{\varepsilon}^{\text{el}}, \tag{6}$$

where λ_1, and λ_2 are Lamé parameters. As per the SOVS constitutive model, the stress is related to the inelastic strain rate as follows [8]:

$$\underline{\sigma} = 2\eta_0 \left[\phi \underline{\dot{\varepsilon}}^{\text{in}} + \left(\psi - \frac{1}{3}\phi \right) \dot{e} \underline{\mathrm{I}} \right] + \sigma_{\text{s}} \underline{\mathrm{I}}, \tag{7}$$

where η_0 is the (temperature-dependent) viscosity of a fully dense material. The sintering stress σ_{s}, normalized shear viscosity ϕ, and bulk viscosity ψ depend on the relative density:

$$\sigma_{\text{s}} = \frac{3\alpha_{\text{s}}}{r_{\text{p}}}\rho^2, \quad \phi = \rho^2, \quad \psi = \frac{2}{3}\frac{\rho^3}{(1-\rho)}, \tag{8}$$

where α_{s} is the surface tension and r_{p} is the median radius of the powder particles.

2.3 Weak form and solution methodology

The weak form of the transient conduction, governed by (2), with a scalar test function δT and using the Backward-Euler scheme for its time-integration takes the following form:

$$\int_\Omega \left(T^{(n+1)} - T^{(n)} \right) \delta T d\Omega + \alpha_{\text{T}} \Delta t \int_\Omega \nabla T^{(n+1)} \cdot \nabla \delta T d\Omega = 0, \tag{9}$$

where Δt is the time-step, and $T^{(n)}$ and $T^{(n+1)}$ are the temperature field at the previous and present time-step, respectively. Building on (9) and the weak formulation of the mechanical part of a slightly different problem in [13], the weak form of the global coupled system, i.e., the thermo-mechanical problem at hand, is given by:

$$\int_\Omega \underline{\sigma}(u, T, [\text{history}]) : \underline{\varepsilon}(\delta u) d\Omega + \int_\Omega \left(T^{(n+1)} - T^{(n)} \right) \delta T d\Omega$$
$$+ \alpha_{\text{T}} \Delta t \int_\Omega \nabla T^{(n+1)} \cdot \nabla \delta T d\Omega = 0, \tag{10}$$

where δu is a vector test function.

To solve the above non-linear system for u and T, we use an outer Newton solver. The assembly of the residual vector and the tangent stiffness matrix is not trivial as the Cauchy stress evaluation is not straightforward due to the strain-rate dependence of the stress in the SOVS model. Internal variables, such as stress, relative density, and strains from previous time instants are stored as history parameters. An implicit scheme is used to evaluate these variables at the present time step. Unlike displacement and temperature, which are evaluated at the nodal points, these history parameters are evaluated at the quadrature points. In order to evaluate the increment of the stress at each quadrature point, an inner Newton solver is employed to solve for the increments in the elastic component of the strain and the volumetric strain rate. For more details of the inner Newton solver implementation and incremental updates of the internal variables, see [26].

3 SURROGATE MODEL

In this section, we discuss the details of the reduced-order modelling framework used in this work. To reduce the computational burden of the sintering simulations in the multi-query context, a reduced-order model is constructed using Proper Orthogonal Decomposition (POD) and Gaussian Process Regression (GPR) [12]. We refer to such a reduced-order model as POD-GPR in the sequel. In the following subsections, we briefly discuss POD and GPR techniques, and how they are used together to construct an efficient reduced-order model.

3.1 Proper Orthogonal Decomposition

Given a parametrized PDE, the solution manifold denoted by $\mathcal{M} = \{u(\cdot; \mu) : \mu \in \mathcal{P}\}$ is composed of all the solutions of the PDE for different parameter values μ in the parameter space $\mathcal{P}$. Generally, an exact solution of the PDE of interest is unavailable, and a finite-element approximation is considered the *truth* solution. The number of degrees of freedom of the finite element approximation, N_{h}, is typically required to be very large for an accurate solution approximation. Using the POD algorithm, a low-dimensional basis for the solution manifold is constructed. To generate this reduced basis, a collection of solution snapshots at a discrete parameter set is first used to construct the snapshot matrix $\mathbf{S} = [\mathbf{u}(\mu^{(1)})|\mathbf{u}(\mu^{(2)})|....|\mathbf{u}(\mu^{(N_{\mathrm{p}})})]$. Subsequently, given an inner product matrix $\mathbf{X}$, we employ the singular value decomposition of the matrix $\mathbf{X}^{1/2}\mathbf{S} = \mathbf{U}\mathbf{\Sigma}\mathbf{Z}^{\mathrm{T}}$, where $\mathbf{U}$ and $\mathbf{Z}$ are orthogonal matrices, and $\mathbf{\Sigma}$ is a diagonal matrix containing the singular values in the decreasing order. The Schmidt-Eckart-Young theorem states that the truncation of $\mathbf{X}^{-1/2}\mathbf{U}$ to the first L columns results in the minimum projection error in the Euclidean norm amongst all possible L-dimensional basis, i.e., the first L columns of $\mathbf{X}^{-1/2}\mathbf{U}$ denoted by $\mathbf{V} = \arg\min_{W \in \mathbb{R}^{N_{\mathrm{h}} \times L}} \sum_{i=1}^{N_{\mathrm{p}}} ||\mathbf{u}(\mu^{(i)}) - \mathbf{W}\mathbf{W}^{\mathrm{T}}\mathbf{X}\mathbf{u}(\mu^{(i)})||_{\mathbf{X}}^2$ [21]. Given the reduced basis, the approximate solution vector for any (new) parameter value is given as $\tilde{\mathbf{u}}(\mu) = \sum_{l=1}^{L} \mathbf{V}_l(\mathbf{u}_{\mathrm{rb}}(\mu))_l$. The coefficients $\mathbf{u}_{\mathrm{rb}}(\mu)$ can be evaluated by solving a reduced problem; see Chapter 3, [21] for the mathematical representation of a classical reduced-order model. However, for nonlinear problems, assembly of this reduced problem is of full-order dimension and, thus, expensive; see Chapters 3, 10, and 11 in [21]. In this work, we circumvent this problem using a regression model trained with the dataset $\{(\mu, \mathbf{V}^{\mathrm{T}}\mathbf{X}\mathbf{u}(\mu)) \, \forall \mu \in \mathcal{P}_{\mathrm{tr}}\}$, where $\mathcal{P}_{\mathrm{tr}}$ is the training parameter space. Here, we use Gaussian process regression to build separate regressors for each coefficient.

3.2 Gaussian Process Regression

Gaussian process regression (GPR) [28] is a non-parametric probabilistic regression model. In GPR, we assume a Gaussian process (GP) prior characterized by mean and covariance functions. The mean function is usually chosen to be either zero or the mean of the training dataset; see Section 4.1 for more details. The selection of the covariance function, also called the kernel function, encodes a desired structure to the GP model. The Radial Basis Function (RBF) kernel is the most widely used covariance function for the GP. It results in very smooth (infinitely differentiable) functions. However, the POD coefficients for which we build the regressors are not necessarily smooth and, hence, we use a different kernel function - *Matern functions*. The class of Matern functions is a generalization of the RBF kernel with an additional positive parameter ν that controls the smoothness of the function. We obtain rougher functions from GP with the Matern kernel using lower values of ν, with $\nu \to \infty$ recovering the RBF kernel. The GP using the Matern kernel with $\nu = 5/2$ produces functions that are twice differentiable. Here, we use the automatic relevance determination (ARD) Matern 5/2 kernel given by:

$$k_\theta(x, x') = \sigma_{\mathrm{f}}^2 \left(1 + \sqrt{5}r + \frac{5}{3}r^2\right) \exp\left(-\sqrt{5}r\right), \quad \text{with } r = \sqrt{\sum_{m=1}^{d} \frac{(x_m - x'_m)}{\ell_m^2}},$$

where d is the dimension of the input parameter space and $\theta = (\sigma_{\mathrm{f}}, \ell_1, ..., \ell_d)$ are the hyperparameters of the kernel function. These hyperparameters are obtained by maximizing the log-marginal-likelihood. Using a different length scale ℓ_m for different input parameters enables us to automatically determine the relevance (ARD) of these parameters.

Due to its probabilistic nature, GPR provides empirical confidence intervals for its prediction which can be used to aid in the active data selection. With this in mind, instead of using the data from the entire training parameter space, we choose the training data based on an active learning strategy; see [12] for the related details. This is done by hierarchically increasing the training data for all L GPR models $\hat{\pi}_{\mathrm{GP}} : \mu \to \mathbb{R}^L$. Using the empirical standard deviation, $\mathrm{sd}[(\hat{\pi}_{\mathrm{GP}}(\mu))_l]$, provided by these GPR models, an error indicator of the approximate solution can be evaluated as follows:

$$\eta(\mu) = \sqrt{\sum_{k=1}^{N_h} \sum_{l=1}^{L} \mathbf{V}_{kl}^2 \mathrm{sd}[(\hat{\pi}_{\mathrm{GP}}(\mu))_l]^2}, \tag{11}$$

and subsequently used to inform on the new training sample selection as described below:

$$\mu_{M+1} = \arg\max_{\mu \in \mathcal{P}_{\mathrm{tr}}} \eta(\mu). \tag{12}$$

To summarize, using POD to obtain the basis and GPR to compute the coefficients corresponding to the extracted (dominant) basis, we have all the ingredients to construct a fast and sufficiently accurate approximation to the high-fidelity solution.

4 NUMERICAL EXPERIMENTS

In this section, we describe the performance of POD-GPR in accelerating the evaluation of the displacement field during the sintering process of the 3D ZnO compact. We investigate
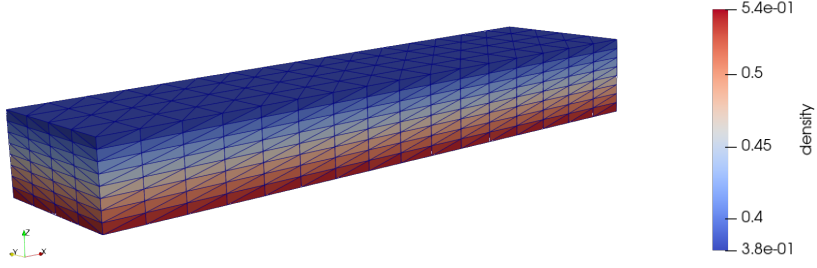
Figure 1: Domain, mesh, and initial relative density distribution.

the results for a two-parameter viscosity function; see Section 4.1 for the parametrization. All the computations presented here are performed on an Intel Core i7-10750H CPU @ 2.6GHz with 32GB of RAM using Python 3.6.9. The full-order FE simulations are performed using the FEniCS library [18], and GPy [10] was used for training the Gaussian process model.

Remark 4.1 *In this work, we restrict our discussion to a non-intrusive reduced-order model constructed to accelerate the evaluation of the displacement field. Similar reduced-order models can be constructed for other fields, such as temperature, density, stress, etc.*

4.1 Problem Setup

A box-shaped powdered compact of $2\ \mu m$ ZnO particles with dimensions D = 16 mm, W = 4 mm, and H = 2 mm is sintered; see Figure 1 for the schematic illustration. We consider the sintering of the 3D compact with a non-uniform density distribution. In particular, the initial relative density of the compact varies linearly in the z-direction with $\rho = 0.38$ on the top surface and $\rho = 0.54$ on the bottom surface. The initial temperature of the compact is uniformly set to 500 K. The heating behavior during the sintering process is modeled as a constant temperature boundary condition on all the boundaries of the computational domain. This temperature profile increases linearly in time from 500 K to 1500 K in 500 seconds,
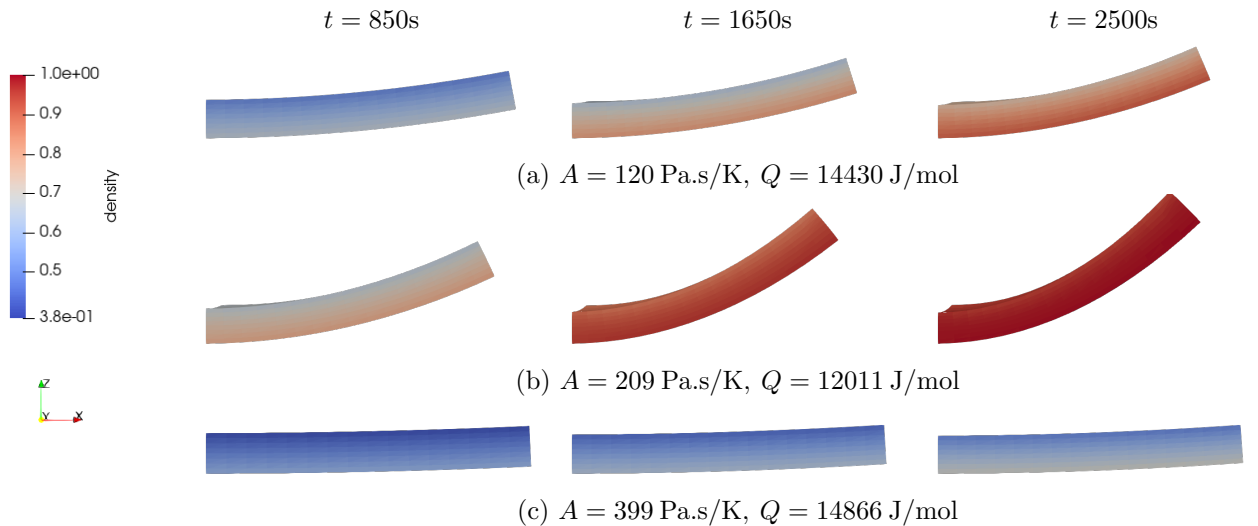

(a) $A = 120\,\mathrm{Pa.s/K},\ Q = 14430\,\mathrm{J/mol}$

(b) $A = 209\,\mathrm{Pa.s/K},\ Q = 12011\,\mathrm{J/mol}$

(c) $A = 399\,\mathrm{Pa.s/K},\ Q = 14866\,\mathrm{J/mol}$

Figure 2: Displacement and density at $t = 850$s (first column), $t = 1650$s (second column), $t = 2500$s (third column) for different parameter values. The color bar reflects density values.

7

and then the temperature is held at 1500 K for additional 2500 seconds. For the mechanical boundary conditions, the material is fixed at the origin. Furthermore, we consider symmetry boundary conditions at $x = 0$ and $y = 0$ planes. The following material properties of ZnO - Lamé parameters: $\lambda_1 = 127.62$ GPa, $\lambda_2 = 51.62$ GPa, surface tension: $\alpha_s = 1.27$ N/m, and thermal diffusivity: $\alpha_T = 2$ mm^2/s - are used in the conducted numerical experiments. The viscosity in the SOVS model is considered a function of the temperature. For the sintering of the ZnO particulate ceramic, we use an Arrhenius-type viscosity function [24] of the form

$$\eta_0(T) = ATe^{\left(\frac{Q}{RT}\right)}, \tag{13}$$

where R $= 8.314$ J/(mol.K) is the universal gas constant. Here, we consider the pre-exponential factor $A \in [80\text{Pa.s/K}, 400\text{Pa.s/K}]$ and the activation energy $Q \in [12\text{kJ/mol}, 16\text{kJ/mol}]$ as model parameters. The relative density and displacement for different values of (A, Q) at different times are shown in Figure 2. It can be observed that as the material sinters it shrinks, but the rate of sintering depends on the relative density. The shrinkage is faster at a lower density which is at the top surface and, hence, the material bends upwards. The parameter-dependent viscosity also affects the rate of the sintering. At higher values of viscosity, the sintering rate is slower. Furthermore, the viscosity increases with an increase in either A or Q.

We prepare a dataset of solutions evaluated at 200 different values of (A, Q) sampled using the Halton sequence sampling procedure [14] with bases 2 and 3, respectively, and the finite element method. This pseudo-random sampling procedure samples the parameter space more evenly compared to the random sampling from a uniform distribution. The obtained dataset is then split into two - one for the training (120 parametric solutions) and the other for the testing (80 parametric solutions). Each solution has 50 snapshots corresponding to different times with constant time intervals (here, 50s). The snapshot matrix required for computing the POD basis is constructed with these 120×50 snapshots. We treat time as a parameter for the POD-GPR i.e., the dimension of the input parameter space d is 3 (i.e., A, Q, t). Hence, the Cartesian product of the 120 training full-order model parameter values with the time values forms the training parameter space, $\mathcal{P}_{\text{tr}}$, for the POD-GPR. We choose $L = 20$ which corresponds to the

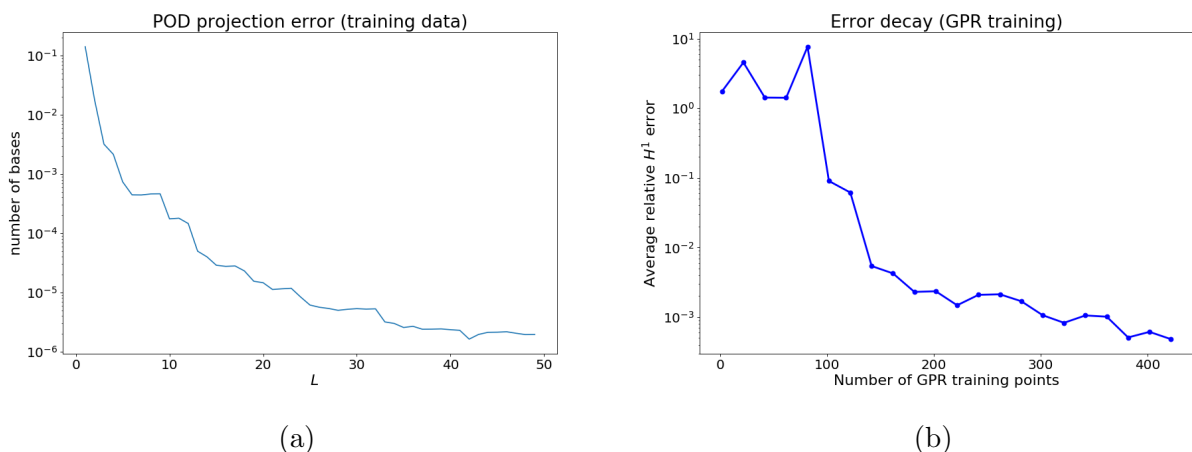(a)   (b)

Figure 3: (a) Decay of POD projection error of the training data with the dimension of POD basis (b) Average error decay with the number of training points for the GPR.
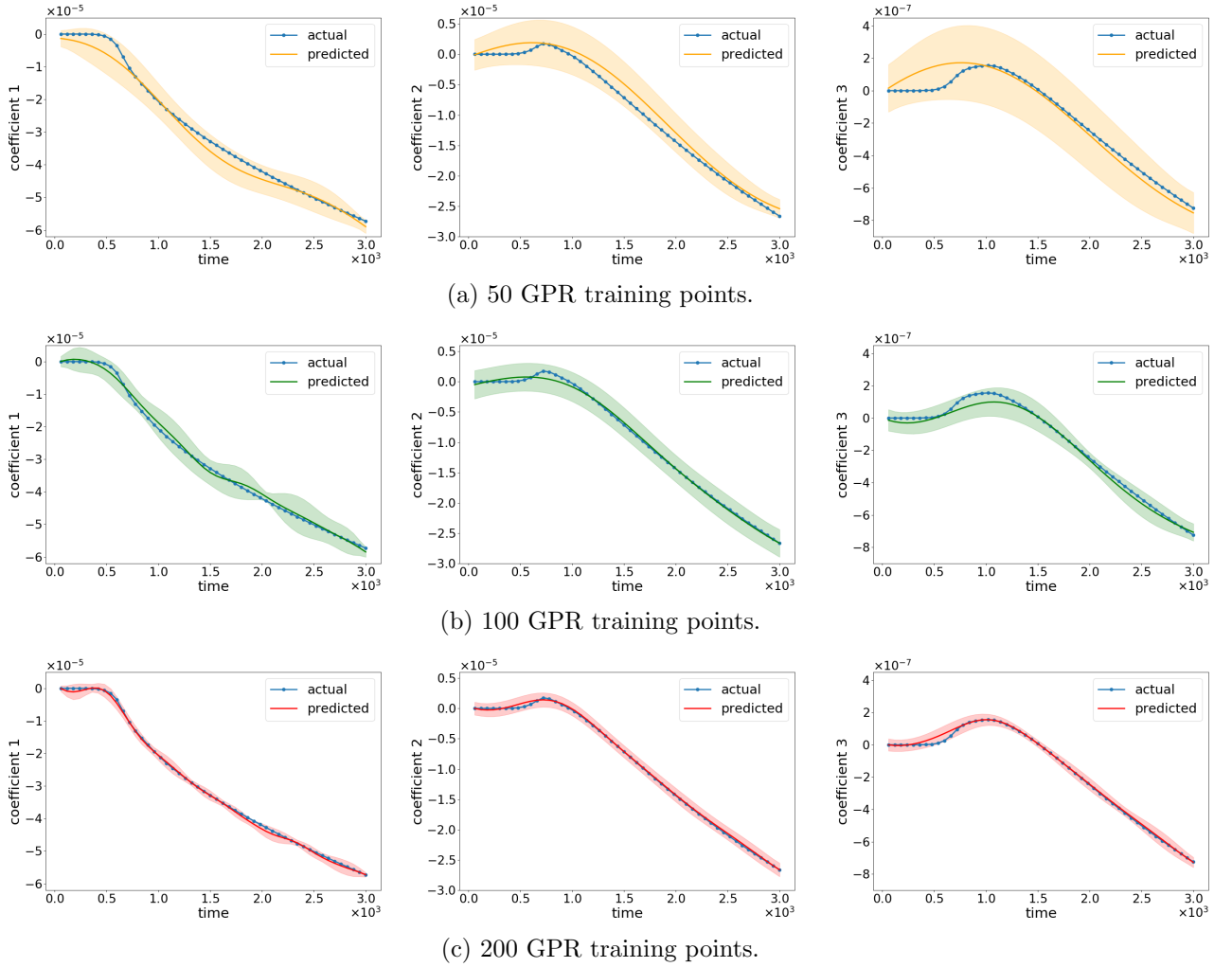
(a) 50 GPR training points.

(b) 100 GPR training points.

(c) 200 GPR training points.

Figure 4: Online GPR coefficient prediction versus the actual POD coefficient.

relative projection (L^∞) error below 1e-5; see Figure 3a. Before training the GPR model we scale and translate the input parameter values and the coefficients such that they have zero mean and unit variance. Subsequently, the mean function for the GPR model is chosen to be zero. The GPR model is trained along with the active learning strategy until the average relative H^1 error goes below an error tolerance $\varepsilon_{\mathrm{GP}} = 5 \times 10^{-4}$.

4.2 Numerical Results

Figure 3b shows a general decaying trend of the average relative error on the test dataset as the number of training data points for the GPR is increased. With just 420 training points from the parameter pool of 120×50 training dataset, the average relative error for the approximate solution generated by the POD-GPR model is below 5e-4. Figure 4 shows the comparison of the GPR prediction against the *true* POD coefficients. For brevity, the comparison is shown only for a particular model parameter value versus time. It can be seen that with an increase in the number of the GPR training points, the GPR model predicts the coefficients more accurately and the empirical standard deviation of the prediction decreases. Also, the active learning

9

strategy chooses training points that prioritize improving the prediction of the coefficients corresponding to the most dominant POD basis over the coefficients corresponding to the (relatively) less dominant basis. Table 1 summarizes the offline computational time required for constructing the reduced-order model using POD-GPR. In total, 4.91 hours are needed in the offline phase. The reduced-order model thus generated is able to compute the approximate solution for any new parameter value in 38.8 ms which is 1675 (= 65 s/38.8 ms; see Table 1) times faster. The offline cost will increase as the full-order simulations get more expensive, but the online time can still remain low resulting in even more speed-ups than the one reported above. Nevertheless, for a wider parameter range, the reduced-order model might need more POD basis functions and more GPR training points, leading to potentially higher online costs.

Table 1: Offline and Online costs.

Cost of computing 200 full-order solutions	65s × 200 = 3.61h
Cost of computing POD basis	38.6 s
GPR training time	78 min
Online time to evaluate solution at new parameter value	38.8 ms

5 CONCLUSIONS

In this work, we successfully accelerated the sintering simulations in a multi-query scenario achieving a speed-up of about $1700\times$ in the online phase compared to the full-order simulations. This acceleration will aid in performing design, optimization, process control, and inverse estimation where numerous simulations for different parameter values are required. Since POD-GPR is completely data-driven and does not require access to the underlying numerical methods used for simulations, it can be used in conjunction with any commercial FEM software. Also, the active learning strategy employed in this work enables faster GPR training, since it requires less number of training points. However, POD-GPR requires numerous full-order computations for both construction of the POD basis and the training of the GPR model. Furthermore, the amount of training data required for the GPR increases drastically with the dimension of the input parameter, thus making this method unsuitable in the high-dimensional parameter space. In the future, we will address these aforementioned issues. Moreover, we will develop a reduced-order model for much more realistic values of the activation energy, and validate the predicted viscosity function against the one obtained in the lab experiment.

REFERENCES

[1] Bordia R.K., Kang S.J.L. and Olevsky E.A. Current understanding and future research directions at the onset of the next century of sintering science and technology. *J. Am. Ceram. Soc.* (2017) **100(6)**:2314-2352.

[2] Chatterjee A., Campbell T., Kalia R.K., Nakano A., Omeltchenko A., Tsuruta K., Vashishta P. and Ogata S. Parallel molecular dynamics simulations of high temperature ceramics. *J. Eur. Ceram. Soc.* (1999) **19(13-14)**:2257-2264.

[3] Chen W., Wang Q., Hesthaven J.S. and Zhang C. Physics-informed machine learning for reduced-order modeling of nonlinear problems. *J. Comput. Phys.* (2021) **446**:110666.

[4] Cicci L., Fresca S. and Manzoni A. Deep-HyROMnet: A deep learning-based operator approximation for hyper-reduction of nonlinear parametrized PDEs. *J. Sci. Comput.* (2022) **93(2)**:57.

[5] Desktop Metal: *Live Sinter* https://www.desktopmetal.com/products/livesinter

[6] Favoretto B., De Hillerin C.A., Bettinotti O., Oancea V. and Barbarulo A. Reduced order modeling via PGD for highly transient thermal evolutions in additive manufacturing. *Comput. Methods Appl. Mech. Eng.* (2019) **349**:405-430.

[7] German R. *Sintering: from empirical observations to scientific principles.* Butterworth-Heinemann, (2014).

[8] Giuntini D., Chen I.W. and Olevsky E.A. Sintering shape distortions controlled by interface roughness in powder composites. *Scr. Mater.* (2016) **124**:38-41.

[9] Giuntini D., Olevsky E.A., Garcia-Cardona C., Maximenko A.L., Yurlova M.S., Haines C.D., Martin D.G. and Kapoor D. Localized overheating phenomena and optimization of spark-plasma sintering tooling design. *Materials* (2013) **6(7)**:2612-2632.

[10] GPy: *Gaussian process framework in Python* http://github.com/SheffieldML/GPy (2012).

[11] Grepl M.A., Maday Y., Nguyen N.C. and Patera A.T. Efficient reduced-basis treatment of nonaffine and nonlinear partial differential equations. *ESAIM: Math. Model. Numer. Anal.* (2007) **41(3)**:575-605.

[12] Guo M., and Hesthaven J. S. Reduced order modeling for nonlinear structural analysis using Gaussian process regression. *Comput. Methods Appl. Mech. Eng.* (2018) **341**:807-826.

[13] Hansbo A. and Hansbo P. A finite element method for the simulation of strong and weak discontinuities in solid mechanics. *Comput. Methods Appl. Mech. Eng.* (2004) **193(33-35)**:3523-3540.

[14] Kocis L. and Whiten W.J. Computational investigations of low-discrepancy sequences. *ACM Trans. Math. Softw.* (1997) **23(2)**:266-294.

[15] Kruth J.P., Wang X., Laoui T. and Froyen L. Lasers and materials in selective laser sintering. *Assem. Autom.* (2003) **23(4)**:357-371.

[16] Leonard K., Deibert W., Ivanova M.E., Meulenberg W.A., Ishihara T. and Matsumoto H. Processing ceramic proton conductor membranes for use in steam electrolysis. *Membranes* (2020) **10(11)**:339.

[17] Little C. and Farhat C. Nonlinear Projection-Based Model Order Reduction in the Presence of Adaptive Mesh Refinement. *AIAA SCITECH Forum* (2023) 2682.

[18] Logg A., Mardal K.A. and Wells G. *Automated solution of differential equations by the finite element method: The FEniCS book.* Springer Science & Business Media, Vol. 84,(2012)

[19] Lu Y., Jones K.K., Gan Z. and Liu W.K. Adaptive hyper reduction for additive manufacturing thermal fluid analysis. *Comput. Methods Appl. Mech. Eng.* (2020) **372**:113312.

[20] Olevsky E. A. Theory of sintering: from discrete to continuum. *Mater. Sci. Eng.: R: Rep.* (1998) **23(2)**:41-100.

[21] Quarteroni A., Manzoni A. and Negri F. *Reduced basis methods for partial differential equations: an introduction.* Springer (Vol. 92), (2015).

[22] Radingoana P.M., Guillemet-Fritsch S., Olubambi P.A., Chevallier G. and Estournès C. Influence of processing parameters on the densification and the microstructure of pure zinc oxide ceramics prepared by spark plasma sintering. *Ceram. Int.* (2019) **45(8)**:10035-10043.

[23] Reiterer M.W. and Ewsuk, K.G. An analysis of four different approaches to predict and control sintering. *J. Am. Ceram. Soc.* (2009) **92(7)**:1419-1427.

[24] Reiterer M.W., Ewsuk K.G. and Argüello J.G. An Arrhenius-Type Viscosity Function to Model Sintering Using the Skorohod–Olevsky Viscous Sintering Model Within a Finite-Element Code. *J. Am. Ceram. Soc.* (2006) **89(6)**:1930-1935.

[25] Rojek J., Nosewicz S., Maździarz M., Kowalczyk P., Wawrzyk K. and Lumelskyj D. Modeling of a sintering process at various scales. *Procedia Eng.* (2017) **177**:263-270.

[26] Shi H., Giuntini D., van Dommelen H., Geers M.G. and Remmers J.J. Efficient modelling of ceramic sintering processes: Application to bilayers and membranes. *J. Eur. Ceram. Soc.* (2023) **43(11)**:4939-4949.

[27] Sleeman M.K. and Yano M. Goal-oriented model reduction for parametrized time-dependent nonlinear partial differential equations. *Comput. Methods Appl. Mech. Eng.* (2022) **388**:114206.

[28] Williams C. and Rasmussen C. Gaussian processes for regression. *Adv. Neural Inf. Process. Syst.* (1995) **8**.

[29] Yabansu Y.C., Rehn V., Hötzer J., Nestler B. and Kalidindi S.R. Application of Gaussian process autoregressive models for capturing the time evolution of microstructure statistics from phase-field simulations for sintering of polycrystalline ceramics. *Model. Simul. Mater. Sci. Eng.* (2019) **27(8)**:084006.